Analysis of gravity effects during binary alloy directional solidification by comparison of microgravity and Earth experiments with in situ observation

Nathalie Bergeon, Guillaume Reinhart, Fatima L. Mota, Nathalie Mangelinck-Noël, Henri Nguyen-Thi

Analysis of gravity effects during binary alloy directional solidification by comparison of microgravity and Earth experiments with *in situ* observation

Nathalie Bergeon[1,a], Guillaume Reinhart[1], Fatima L. Mota[1], Nathalie Mangelinck-Noël[1], Henri Nguyen-Thi[1,b]

[1]*Aix Marseille Univ, Université de Toulon, CNRS, IM2NP, Avenue Escadrille Normandie Niemen, 13397 Marseille cedex 20, France*

[a]*e-mail : nathalie.bergeon@im2np.fr*

[b]*e-mail : henri.nguyen-thi@im2np.fr*

Corresponding authors : Nathalie Bergeon (nathalie.bergeon@im2np.fr) and Henri Nguyen-Thi (henri.nguyen-thi@im2np.fr), Aix Marseille Univ, Université de Toulon, CNRS, IM2NP, Avenue Escadrille Normandie Niemen, 13397 Marseille cedex 20, France

Abstract: Under terrestrial conditions, solidification processes are influenced to a large degree by the gravity effects such as natural convection or buoyancy force, which can dramatically modify the final characteristics of the grown solid. In the last decades, the coupling of *in situ* observation of growth from the melt, that enables the study of microstructure formation dynamics, and microgravity experimentation, that allows to approach diffusive conditions, has been implemented for both transparent and metallic materials. The results of these investigations enable to test the validity of advanced solidification theories, to validate or develop numerical models and sometimes to reveal unexpected phenomena. The aim of this paper is to present a selection of conclusive experiments obtained with this combined approach in our group to highlight the gravity effects by a comparative study of experiments carried out on earth and in microgravity conditions.

1. Introduction

1.1. Solidification microstructures

The fundamental understanding of microstructure formation during solidification from the melt is crucial since microstructures are the strategic link between elaboration and properties of materials [1, 2]. During industrial processes, such as casting or welding, solidification or crystal growth can occur in two basic modes: *(i)* free growth in which an initially spherical or globular crystal becomes unstable during growth and gives rise to equiaxed dendritic grain [3]. As a result, the final solid consists of a huge number of grains randomly oriented, with uniform and isotropic properties [4, 5]. *(ii)* The second mode is directional growth in which an alloy is solidified unidirectionally in a temperature gradient G. In this case, the final product consists of a limited number of elongated grains, with anisotropic properties. Creep-resistant turbine blades and vanes are produced by directional solidification, enabling an accurate control of the microstructure and the manufacturing of single-crystal parts [6, 7]. For fixed alloy composition (defined by the solute concentration C_0), and temperature gradient G, like in a Bridgman-Stockbarger furnace, the solid-liquid interface undergoes transitions from planar to cellular to dendritic patterns as the growth velocity is increased [8, 9]. For cellular growth, significant solute and temperature field interactions occur between neighboring cells in the array, which strongly influence cell shape and tip characteristics (radius, temperature and composition) [9-11]. For dendritic growth in directional solidification, steady-state dendrite tip characteristics have been predicted for a dendritic array in which solute interaction between the neighboring dendrites is negligible. In this case, the shape of the dendrite tip is shown to be very close to a parabola [9, 12-14].

1.2. Convection effects in Bridgman growth

Despite the importance of cellular or dendritic microstructures in commercial products, many key fundamental aspects that govern microstructural scales and accompanying segregation pattern have not been clearly established [15]. In this paper, we focus on the impact of gravity-driven phenomena on the microstructure dynamics during vertical Bridgman growth because most directional solidification experiments are carried out in this arrangement. The first and most studied gravity effect is natural or buoyancy-driven convection that occurs practically in every melt growth system because melt density varies both with the temperature distribution and the solute concentration. [16-19]. Vertical gradients of melt density can be either stabilizing or destabilizing regarding convection, however, any gradient of melt density that is not exactly parallel to the gravity vector can potentially cause the onset of buoyancy flow so that natural convection is expected in all experiments. To avoid natural convection in the melt, it seems reasonable to ensure that the density gradient is solutally stable, i.e. vertical everywhere and with the heaviest material being at the bottom. This situation is more or less approached when growth takes place upwards in an alloy system in which the rejected solute is denser than the solvent like for Al-Cu alloys. Actually, even in this experimental configuration, flow patterns adjacent to the front are known to develop as a result of residual horizontal density gradients [20-23]. A second important gravity-driven phenomenon is the buoyancy forces acting on solid, which can be dendrite fragments [24, 25], equiaxed grains [26, 27] but also secondary dendrite arms [28-30]. Actually, densities of solid crystals and of the surrounding melt are almost always different, so that a non-zero force acts on the growing solid. As a result, free solid fragments are expected to float or to sediment during growth process.

Gravity-driven effects can be strongly damped during solidification experiments by reducing sample dimensions and performing solidification horizontally [31]. Diffusive growth conditions can be nearly achieved in very thin flat samples of thickness in the 10 µm range or

in cylindrical capillaries of inner diameter of less than in 1 mm for metallic alloys [32]. Suppressing convection motions in bulk samples (also referred to as three-dimensional, or 3D, samples) during solidification is a much more challenging task. Numerous experiments in microgravity conditions have shown that microgravity (µg) environment is a unique and efficient way to eliminate buoyancy and convection to provide benchmark data for the validation of models and numerical simulations [31]. For these reasons, materials science and more particularly solidification of metal alloys has been a prominent topic of research in microgravity field since the early stages of microgravity experimentation. Considering the large characteristic times of diffusion-controlled growth, long-duration microgravity conditions are required. Accordingly, dedicated *in situ* solidification facilities have been installed on board of various space orbiting platforms (e.g. the now retired space shuttles) and more recently in the International Space Station (ISS) or sounding rocket (MASER). In microgravity environment, transport phenomena are essentially diffusive and buoyancy forces vanish, which highly simplifies the experimental analysis by decoupling the phenomena at stake as for example solute distribution in the melt that is modified when convection is present or motion of grain or dendrite fragment due to buoyancy force. Moreover, microgravity experimentation allows a more direct and precise comparison with advanced theoretical models [33-35]. Indeed, most of the current theoretical models do not consider the convective phenomena or grain motion as they primarily aim at exploring the mechanisms of solidification, development and selection of the microstructure; this fundamental basis is required to add the very complex influence of fluid flow that also needs to be characterized experimentally. Even in the case of models or numerical simulations that have been developed to consider convection, a first validation step restricted to diffusive conditions is much valuable because of the complex interplay of convection with all other mechanisms at stake. Besides, comparative studies of solidification experiments performed in normal gravity (1g) with experiments conducted either in

microgravity conditions [20, 36] or enhanced gravity [37-40] can be very helpful to enlighten the effects of gravity. The influence of gravity on the structural transitions (dendritic/eutectic and cell-dendrite transitions), the difference between the space and ground samples primary spacing and the dendritic array morphology were thoroughly analyzed, showing a strong impact of the transport mode in the melt. In this paper, we present a review of several successful real-time solidification experiments under microgravity, in bulk transparent (visible-light optical diagnostics) and metallic (microfocus X-ray radiography) alloys. The highlights that are presented include spacing selection for cells and the dynamics of a planar front in bulk samples, the influence of microscale flow structures on the dynamics of columnar dendrite tips, and dendrite fragment generation in metallic samples. Most of these results have been published before but the value and appeal of this paper are that it gathers and reviews the key findings on gravity effects obtained by using *in situ* and real-time observation during directional solidification of binary alloys.

2. *In situ* observation of microstructure formation

The fundamental understanding of solidification microstructure formation in alloys is intrinsically difficult, insofar as it involves simultaneously a great number of phenomena, at different time and spatial scales [9]. Moreover, microstructure pattern selection occurs under dynamic conditions of growth in which the unstable pattern goes through the process of reorganization into a rather periodic array. The progress of *in situ* and real-time observation of the microstructure formation represents a critical step in the field of solidification as it provides a detailed knowledge of the entire time-evolution of the interface pattern [15, 31].

2.1. Transparent alloys

The first breakthrough in experimental solidification research was the utilization of transparent organic materials proposed by Jackson and Hunt in 1965 [41]. These organic materials can solidify with typical cellular and dendritic morphology like metals during solidification. The main advantage of these materials is their transparency, so that the dynamics of the propagating solid-liquid interface can be directly observed with an optical microscope. Binary alloys based on Succinonitrile - SCN ($C_4H_4N_2$) or Carbontetrabromide (CBr_4) are among the most commonly used organic systems for researches of dendritic growth during solidification because of the accurate knowledge of their physicochemical properties and phase diagrams. In addition, the use of very thin samples allows to drastically damp natural convection effects and then to be closer to conditions assumed in the most advanced theoretical models [9, 42-47]. Even if such configurations have led to step forward in understanding the dynamics of solidification, they do not perfectly represent 3D samples. Indeed, quantitative data extracted from 2D systems cannot be extrapolated to 3D ones [48-50] and 3D studies reveal the critical influence of some specific features that are absent or drastically reduced in thin configurations [51, 52]. To eliminate the significant convection unavoidable during growth of 3D organic samples, the reduced-gravity environment of space is mandatory.

The present results rely on experiments performed in the Directional Solidification Insert (DSI) dedicated to *in situ* and real-time characterization of the dynamical selection of the solid-liquid interface morphology in bulk samples of transparent materials. It was developed by the French Space Agency (CNES) in the framework of the DECLIC project (DEvice for the study of Critical Liquids and Crystallization). The DECLIC facility was installed onboard the International Space Station (ISS) as part of a joint NASA/CNES research program. Two series of microgravity experiments were performed in 2010-2011 and in 2017-2018 on samples of different compositions (succinonitrile based alloys with respectively 0.24 and 0.46 wt% of camphor).

In the DECLIC-DSI (Directional Solidification Insert), the experimental cartridge is inserted in a Bridgman furnace. The cartridge comprises a quartz crucible and a system of volume compensation to accommodate the specimen volume variations associated with phase changes. The cylindrical crucible has an inner diameter of 10 mm and a length that enables about 10 cm of solidification, allowing the study of the whole development of extended patterns from their initial stages up to the steady growth regime.

Figure 1 is a scheme of the optical observation modes. The main observation mode (axial) takes advantage of the complete transparency of the experimental cartridge: the light coming from LEDs passes through the cartridge from the bottom to the top, crossing the interface whose image is formed on a CCD camera. An example of dendritic pattern imaged with this diagnostic is given on the top-right of the figure. Such top-view images of the interface are used to study array dynamics and characteristics. On the same axis, a Mach-Zehnder interferometer with a He-Ne laser produces interferometric images used for three-dimensional reconstruction of microstructures [53, 54]. Additionally, the transverse observation mode provides side-view images of the interface, which allow a real-time characterization of interface motion and macroscopic shape (see example of dendritic pattern imaging with this diagnostic on the bottom-right of fig.1). Solidification was performed by pulling the experimental cartridge from the hot zone towards the cold zone at a constant rate V within a range between 0.1 and 30 µm/s. A temperature gradient G ranging from 10 to 30 K/cm was imposed by regulated hot and cold zones, located above and below the adiabatic area where the interface is positioned. Further details about the experimental procedure can be found in previous articles [51, 55].

2.2. Metallic alloys

Real-time observation of the solidification process in non-transparent materials (metals and semiconductors) has been a critical issue for a long time. Standard investigation techniques,

such as quenching or decanting, do not provide the interface evolution over time in 3D, but gives only a frozen picture of the solid microstructure. This difficulty was partly circumvented by applying Peltier interface demarcation technique applied e.g. to the study of faceted growth of semiconductors like Bi-Sb alloys [56, 57]. For deeper insight into metallic-alloy solidification, a major breakthrough was the use of high-brilliance X-ray sources. Indeed, the beam intensity associated with modern synchrotron radiation result in a substantial extension of X-ray imaging capabilities to high spatial and temporal resolutions, allowing one to gain key information on crystal growth-related phenomena that was not available hitherto. Among the different synchrotron radiation X-ray imaging techniques [58], X-radiography is currently the most widely used because it is the simplest one to implement. This technique is based on the local changes in the amplitude of a transmitted X-ray beam due to differential absorption by an inhomogeneous sample [59, 60]. In Al-based alloys, contrast firstly results from segregation of the chemical species and secondly from the difference of density between the solid and liquid phases. Recently, the development of microfocus X-ray sources along with increasingly sensitive detectors has led to vast improvements in the performance of laboratory radiography devices [25, 61-63]. While synchrotron sources mostly provide horizontal parallel beams, a microfocus source delivers a cone-shaped beam, and enables an image magnification up to a factor of 5, depending on the source-to-sample and source-to-detector distances. Figure 2 shows a schematic layout of the XRMON-GF set-up that was developed in the framework of the ESA XRMON project to perform directional solidification with *in situ* X-ray radiography observation in microgravity conditions. A detailed description of the facility has been given in previous papers [25, 64] and only the main features are summarized below. The dimensions of the sheet-like samples were 5 mm in width, 50 mm in length and 0.25 mm in thickness. The sample thickness was chosen to have a good transmission of the X-ray beam and prevent the superimposing of several grains at the same location so that the interpretation of radiographs is

unambiguous. The sample was placed into stainless-steel spacers, sandwiched between two flexible glassy carbon sheets sewn together with a silica thread. The sample-crucible assembly was then installed inside the Bridgman-type furnace. The furnace consists of two identical heaters that are independently regulated by a PID-regulator. This feature allows a temperature gradient *G* to be applied by fixing the temperature of the two zones (fig.2a). During the experiments, the samples were directionally solidified by applying the same cooling rate *R* on both heater elements, ensuring a constant applied temperature gradient *G* during the entire experiment. The furnace enables directional solidification with temperature gradients within the range of 2.5–15 K/mm and cooling rates *R* within the range of 0.01–1.5 K/s. The X-radiography system is based on a microfocus X-ray source with a molybdenum target and a 3 mm focal spot. It provides a photon flux with two peaks of energy at 17.4 keV and 19.6 keV that ensure a good image contrast to study Al-Cu based alloys. The camera system is made of a scintillator plate that converts X-ray radiation to visible light and a digital camera with a CCD sensor. In this work, a Field-of-View (FoV) of about 5×5 mm^2 and an effective pixel size of ~4×4 µm^2 were used and the acquisition rate was 2 frames/second. These spatial and temporal resolutions are sufficient to observe the various steps of the microstructure development from the radiographs. Gray level variations in the radiographs are related to the difference in X-ray absorption in the sample regions, which depends mainly on the local density and composition. Image quality was enhanced by applying an image processing consisting in dividing each recorded frame by a reference picture recorded just before the beginning of the solidification [22]. After image processing, radiographs showed the microstructure formed during the directional solidification. In the case of Al-Cu alloys, liquid regions of high copper concentration appear as dark regions in the images, while α-Al dendritic grains with low copper concentration appear as bright regions (fig.2b).

3. Selected results concerning the solidification in 3D transparent samples

In this section, the microgravity (referred as µg) experiments conducted on a sample of Succinonitrile – 0.24wt% Camphor are compared to Earth (referred as 1g) experiments performed after the return on Earth of the sample. The experimental conditions used were the same for both experiments so that the influence of convection can be emphasized. In the experiments described in the following, two different temperature gradients were used (12 and 19 K/cm) and the pulling rate varies from 0.35 to 30 µm/s.

The transverse observation mode is used to characterize the interface shape, motion and evolution. At rest, the planar solid-liquid interface is located at the liquidus alloy temperature and its shape follows the isotherm shape, usually curved in 3D geometries. Images show that the interface at rest is convex for both temperature gradients, which means that the liquid close to the crucible is hotter than in the center.

Once a pulling rate is applied, the interface temperature decreases and moves closer to the cold zone where isotherms are concave. Moreover, due to the low thermal conductivity of the alloy compared to the quartz crucible, evacuation of latent heat generated during growth mainly occurs through the crucible, thus inducing a temperature radial gradient from the periphery (colder) to the center (hotter) of the crucible. Thus, the interface progressively becomes more concave as velocity increases. Lastly, isotherms are shifted downwards by heat transport in the cartridge, also leading to an increase of concavity. Both effects are roughly proportional to pulling rate as detailed in a previous study [51]. On Earth, the radial temperature gradient induces thermal convection [65]. For convex interfaces, the hotter liquid with lower density located at the periphery is driven upwards by buoyancy, so that a toric convection loop, ascending at the periphery and descending in the center, is formed. For concave interfaces, the liquid in the center is hotter, so that fluid flow rises in the center of the crucible. The fluid flow

direction is schematically represented in the top-left and bottom-right insets of fig.3a, respectively for convex and concave interfaces. Two different aspects of the thermal convection influence will be illustrated in the following. First, we will analyze its effect in terms of pattern development and characteristics; the average primary spacing of microstructures as well as their spatial homogeneity, will be compared on ground and in µg. Second, we will evidence the convection effect on axial macrosegregation.

3.1. Pattern development and characteristics

In a previous work, the microstructure formation was studied starting from the interface at rest until the stationary state, for a temperature gradient of 19 K/cm and pulling rates from 0.5 to 16 µm/s [66]. The original results presented in this work concern a temperature gradient of 12 K/cm and pulling rates ranging from 0.35 to 30 µm/s. The first stages of solidification have fast dynamics with the transient development of microstructure, followed by a stationary state growth characterized by a stable spacing even if the patterns keep evolving in terms of topological order. Detailed description of microstructures, primary spacing evolution and mechanisms of adjustment can be found elsewhere [52].

The first striking point comparing µg and 1g experiments is the shift of morphological stability threshold associated to convection. On ground, the solid-liquid front remains planar for pulling rates up to 1 µm/s, whereas morphological instability occurs below 0.35 µm/s in µg. Such difference was already evidenced theoretically [67, 68] and experimentally [32, 67]. This effect is classically explained considering a diffusive boundary layer in the liquid close to the solid-liquid interface, as initially introduced by Burton, Prim, and Slichter [69]. Fluid flow reduces the thickness of the boundary layer; the concentration ahead of this boundary layer is considered homogeneous, well-mixed at the nominal concentration. Solute conservation then implies the decrease of the liquid solute concentration at the interface compared to pure diffusive conditions. The solute concentration in the solid also decreases since it is determined

by interfacial equilibrium and is then proportional to the concentration in the liquid by the partition coefficient k. The interfacial concentration gradient, which drives the interface instability, is thus reduced inducing a stabilization of the interface and an increase of the critical velocity in the presence of fluid flow on ground.

The average primary spacing variation with pulling rate, for 1g and µg experiments, is given in fig.3a. The interface shapes are given in the insets, thus evidencing two different domains: below V = 4 µm/s, the interface is convex and the primary spacing at 1g is lower than in µg; whereas above 4µm/s, the interface is concave and the primary spacing at 1g is larger than in µg. At 4 µm/s, the interface is macroscopically flat and the average primary spacing is identical in 1g and in µg. It should be reminded here that the macroscopic interface shape is a consequence of the isotherm shape that are curved. The isotherm curvature and thus, the interface shape, is related to its position in the thermal field. The interface adapts to the more concave isotherms as its moves closer to the cold zone. A detailed discussion about the evolution of the interface curvature can be found in [51]. The histogram of the primary spacing (fig.3b) is also comparable. Such results may seem surprising since previous studies on metallic systems pointed out spacing in microgravity larger than on ground with a convergence when the pulling rate increases [20, 36]. The difference comes from the different origin of convection. In the studied transparent system, the radial temperature gradient, and associated concavity, increase with latent heat release, so that fluid flow and its effect increase with pulling rate. In metallic systems, thermal convection stems from the difference of conductivities between the solid and the liquid, which promotes interface convexity. The latent heat effects are negligible because thermal diffusion is fast in metallic samples. When the pulling rate becomes large enough, the effect of fluid flow turns negligible and the primary spacing is no longer affected by fluid flow. The current opposite effect of fluid flow on primary spacing can be attributed to the flow direction, resulting from the concavity or convexity of the interface: in metallic

systems, the liquid sinks in the center and rises on the border, whereas it is the opposite in the presently studied transparent system.

The inversion of the convection effect on primary spacing below and above 4 µm/s (observed in fig.3a) results from the change of flow direction. Below 4 µm/s, the interface is convex and we can use the approach of Lehmann et al. [70] developed for metallic systems (convex interface with a downwards central flow). They propose a relationship between the component of fluid flow velocity $U_{/\!/}$, parallel to the pulling velocity (taken negative for a downwards component) and the primary spacing λ and λ_0, respectively with and without influence of convection:

$$\left(\frac{\lambda}{\lambda_0}\right)^2 = \left(1 - \frac{U_{/\!/}}{V}\right) \quad (1)$$

This equation is valid as long as the right term is positive, so as long as $U_{/\!/} \leq V$. For a convex interface, flow is descending in the center so $U_{/\!/} < 0$ and $\lambda_0 > \lambda$, as observed in experiments in metallic systems and in our case for pulling rates lower than 4 µm/s. We used equation (1) considering $U_{/\!/} > 0$ for upward flows associated to the concave interfaces obtained above 4 µm/s, with $\lambda_0 < \lambda$. Using primary spacing data of fig.3, we can evaluate the fluid flow velocity for the range of pulling velocity: it appears to vary almost linearly with V, starting from $U_{/\!/}$ = -3.9 µm/s at V = 1 µm/s to $U_{/\!/}$ = 20 µm/s for V = 30 µm/s. These results are in good agreement with the ones found in our previous work dealing with a higher temperature gradient [66].

Observing the histograms of primary spacing for V=2µm/s given in fig.3b, we notice that convection not only modifies the average primary spacing, but also enlarges the distribution. This enlargement is the result of spatial microstructure heterogeneity. This is illustrated for example on fig.4 with the comparison of cell size distribution in µg and 1g conditions for V = 4 µm/s (G = 19 K/cm). The corresponding interface shapes for these experiments reveal that the concavity is much larger on ground than in µg. The origin of this difference in interface

curvature is well known: the solute rejected upon solidification is swept by the convection and accumulated at the center for a concave interface, or at the border for a convex interface. The liquid solute concentration then varies along the interface, thus modifying locally the equilibrium temperature of the interface. Accumulation induces a decrease of the interface temperature and a resulting increase of the curvature. The variation of solute concentration along the interface directly affects microstructure formation and selection as it generates a gradient of instability level. On the example of fig.4, on ground, larger cells are observed in the center compared to the border, whereas cell size is more homogeneous in µg. This result is typical of a toric convection ascending in the center and descending at the border, as already reported elsewhere for the same geometries and succinonitrile based alloys [65, 71, 72].

3.2. Macrosegregation

When pulling of the sample at a constant velocity V is initiated, the interface recoils within the temperature frame, and the solute concentration builds up on the liquid side of the interface. This interface motion from rest to its steady state position is referred to as the front recoil. During this stage, the interface velocity increases to reach the pulling velocity in the steady-state. The planar front undergoes the Mullins-Sekerka instability [73, 74] when the solute concentration gradient in front of the interface G_c exceeds the critical value G/m_L, with m_L the alloy liquidus slope. This initial interface dynamics before the destabilization of the planar front can usually be well predicted by the Warren-Langer model [75].

Interface recoil comparisons between results obtained on Earth (1g) and onboard the ISS (µg) for different pulling rates and imposed temperature gradient of 12 K/cm are presented in fig.5. The fast motion observed at the beginning of the solidification is similar on ground and in µg but the interface decelerates earlier on Earth. Whatever the pulling rate is, front recoils

on ground are characterized by the absence of stabilization of the interface position, meaning that instead of reaching a plateau, the interface keeps moving downwards.

Since the interface grows in local thermodynamic equilibrium, solute interfacial composition variations in the liquid induce similar variations of composition in the solid. The solute build-up during planar front recoil, and the subsequent transient development of patterns of cells or dendrites before a steady-state growth regime is reached, is a first cause of axial macrosegregation. If the interface temperature keeps evolving, meaning that steady-state is not reached, an additional source of axial macrosegregation must be considered.

Stabilization (i.e. µg – V = 4 µm/s in fig.5) corresponds to a plateau of concentration reached after the initial transient. It is typical of a purely diffusive mode and most microgravity results follow this tendency. Absence of stabilization corresponds to a characteristic "S-shape" macrosegregation profile, typical of a convecto-diffusive growth mode [76]. This evolution is observed for all ground experiments but also surprisingly for microgravity experiments performed at the lowest pulling rate (i.e. µg - V = 0.5 µm/s in fig.5). For these conditions, an order of magnitude analysis of fluid flow [77, 78] shows that diffusive conditions can only be obtained for a gravity level equal or lower than 10^{-6}g (fig.13 of Mota et al [51]) whereas the actual gravity level during this experiment was much closer to 10^{-3} or 10^{-4}g. The consequence is that the microstructure of the experiments performed at low velocities in µg but for gravity level from 10^{-3} or 10^{-4}g are affected by significant residual convection so that diffusive conditions are not reached on the contrary to higher velocity µg experiments.

4. Examples of results in metal alloys

In this section, the influence of gravity-driven phenomena on columnar growth of Al-20wt%Cu alloys will be presented. We will focus on two issues of great importance for industrial application, namely dendrite fragmentation and plume formation.

4.1. Effect of gravity on dendrite fragmentation

Dendrite fragmentation is a process of detachment of secondary or tertiary dendrite arms from the trunk (or sometimes of the primary trunk itself) that can occur during solidification process. As a consequence, this undesired event disturbs the dendritic growth and can generate defects that are detrimental for the final product. A key question in solidification is to know which mechanisms are at the origin of dendrite fragmentation during dendritic growth. It is now accepted that the most potent effect is the remelting at the neck of dendrite arms due to a local solute increase which modifies the equilibrium temperature [79]. This neck remelting leads eventually to the secondary arm detachment from the primary trunk. Because of its transient characteristics, fragmentation phenomenon is widely studied by synchrotron X-radiography because this technique can reveal solidification dynamics and in particular, the dynamics of the dendrite arm fragmentation and the subsequent behavior of the dendrite fragments after detachment [80, 81]. Of course, X-radiography resolution does not allow to study the details of the fragmentation at the level of the neck due to the required spatial resolution. Nevertheless, it enables to detect the dendrite fragments when they move after their detachment and then to determine accurately the number of events during the solidification process [24, 29]. In such type of experiments carried out using synchrotron sources, the role of gravity could not be rid of because of the horizontal beamline and thus the vertical position of the samples. Consequently, the influence of gravity-driven phenomena (such as natural convection and solid phase buoyancy) on dendrite fragmentation could not be excluded.

To tackle the problem of the influence of gravity-driven phenomena on dendrite fragmentation, a qualitative comparison between experiments performed on Earth [82] and in microgravity conditions on board of MASER-12 sounding rocket [25] was reported in [31]. It has been

pointed out that, in the absence of gravity dendritic fragments were detected only deeply into the mushy, whereas numerous fragmentation events occurred in the upper part of the columnar front zone and subsequently moved upward due to buoyancy. In this paper, a comparative quantitative analysis of those experiments is presented and the effects of gravity on dendrite fragmentation is emphasized. For the sake of relevant comparison, the experiments were carried out with the same solidification parameters (average temperature gradient G = 15 K/mm between the heaters and a cooling rate R = 0.15 K/s), which ease the analysis and give clear conclusions.

Figure 6 displays the time evolution of the interface pattern during the solidification of an Al - 20 wt% Cu alloy in microgravity conditions (first row), and for two reference experiments at normal gravity. The second row depicts the case of horizontal solidification configuration for which the gravity effects are largely reduced. The third row is the upward solidification case for which gravity effects are expected to be the strongest. For the latter, the most important feature is the visible multiple fragmentations observed in the dendritic tip region, at the top of the columnar front (fig.6c). After their detachment, most fragments moved upward due to the buoyancy force because the solid density is lower than the density of the surrounding liquid. Some of those fragments were free to float to the hot region of the sample (white arrows in fig.6c). During their upward motion, the size of the dendrite fragments decreased because they gradually melted, forming a final white cloud, which corresponded to the melting of the aluminum-rich dendritic fragment. A direct consequence of dendrite fragmentation is a strong macrosegregation along the sample because all Al-enriched dendrite fragments were transported by buoyancy forces into the upper part of the sample and mixed in the liquid phase after melting.

For the 1g-horizontal and microgravity experiments, when looking at the mushy zone in details, a few dendrite fragmentations were also observed but about several hundred micrometers below

the dendrite tip position. Of course, these rare events were difficult to be detected as the dendrite fragments remained trapped between dendrites and could only move over very short distance. Moreover, those dendrite fragments moved towards the cold part of the mushy zone, on contrary to dendrite fragments generated at the top-region of the mushy zone. This change in direction motion was ascribed to the downward liquid flow induced by the sample shrinkage [83].

A quantitative analysis of dendrite fragmentation was then performed by determining the number of visible fragments for each experiment. For this characterization, the mushy zone (MZ) was divided in two regions (fig.7a) : *(i)* the top-region of the mushy zone, which is the region just behind the dendrite tips and where the liquid fraction is large, and thus where the effects of gravity are expected to be strong, and *(ii)* the deep mushy zone, which is a region where the liquid fraction tends toward zero, and thus where the effects of gravity are expected to be weak. Figure 7b displays the bar chart drawn from our measurements. The red rectangles correspond to the number of dendrite fragmentation events for the µg experiment, while the blue rectangles are the value for the 1g-upward experiment. With this direct quantitative comparison between 1g and µg experiments, it is thus possible for the first time to enlighten the influence of gravity on fragmentation phenomenon.

The first observation was that, whatever the experiment (in normal gravity conditions or in microgravity environment), the majority of dendrite fragmentations occurs in the top-region of the mushy zone compared to the deep region. This was particularly true when comparing the respective sizes of the two regions. Indeed, only a few rare events were detected in the deep region of the dendritic network and there was no marked difference for fragmentation number between the two experiments. This interesting observation suggested that, when the liquid fraction is very low and solute transport mainly diffusive like in the deep region of the mushy zone, dendrite fragmentation is scarce, in agreement with recent papers published by Liotti *et al.* [81] and Gibbs *et al.* [84]. These two groups have performed similar measurements along

the whole mushy zone and they have found that the maximum of dendrite fragmentation occurs behind the dendrite tips (about 1000 µm in their particular experimental case). The maximum of dendrite fragmentation occurs in the region of the mushy zone where the permeability, which decreases from unity at dendrite tips to zero at eutectic front, allows transport of hot and solute enriched liquid. The mushy zone permeability depends on the primary and secondary dendrite arm spacings and on the solid fraction and can be calculated e.g. by using the Carman-Kozeny relationship [85, 86]. Moreover, the mushy zone permeability also changes depending on flow direction, parallel or normal to the primary dendrite arms.

Figure 7b also emphasizes the marked difference between 1g and µg experiment for the number of fragmentation events in the top-region of the mushy zone. The fragmentation number is four times larger for the 1g experiment compared to the microgravity experiment, which clearly indicates a strong effect of gravity conditions. To explain this marked difference due to the gravity, two reasons can be put forward: *(i)* Firstly, in the top of the MZ, we expect to have natural convection in the inter-dendritic liquid regions due to the solute rejection during solidification. By transporting the rejected solute toward the secondary arm neck, these fluid flows can enhance the local remelting of the neck by changing locally the equilibrium liquidus temperature and thus can increase the fragmentation number (as indicated in fig.8a). *(ii)* Secondly, for Al-20wt%Cu alloy, the buoyancy force that acts on secondary arm causes a torque on the secondary arm (as illustrated in fig.8a), which promotes the dendrite fragmentation, as we showed in [29, 30]. The combination of these two gravity-driven effects can explain the factor four between the fragment amount at 1g-upward and in µg conditions and emphasizes the critical role of gravity on dendrite fragmentation often ignored in models or numerical simulations.

4.2. Impact of solute plumes on dendrite growth

As previously mentioned, natural convection that takes place in the melt is the source of various disturbing effects, which can significantly modify or mask other physical mechanisms because flows in the liquid modify the solute transport in the melt, and generally prevent the formation of steady solidification patterns with uniform features. For Al-20wt%Cu alloy, these effects are very important when solidification is carried out in a vertical configuration and with a temperature gradient parallel to the gravity vector (hereafter referred as 1g-downward). In that arrangement, the temperature field is destabilizing regarding convective instabilities as the hot liquid was below the cold liquid. In addition, the rejected solute (Cu) is heavier than the solvent (Al), yielding the solute to sink due to gravity and amplifying convective flow. In a previous work [87], the influence of solute plumes on the dynamics of columnar dendrite tips was presented in details. The original results presented in the present work concern an experiment carried out on the same refined Al-20wt%Cu alloy sample but with different solidification parameters (G = 7.5 K/mm and R = 0.1 K/s).

Figure 9 depicts a sequence of radiographs showing the representative behavior of this 1g-downward solidification experiment. In this experiment, a porosity defect grew into a hole as visible at the bottom of the FoV and indicated in the first radiograph. The first grains growing from the cold region of the sample and then entering the FoV are visible fig.9b, as well as downward flows of Cu-rich liquid coming from the solidification microstructure and moving towards the bulk liquid (white arrows). These convective plumes are caused by the rejection of heavy solute in the mushy zone during the solidification microstructure formation and were visible long before the appearance of the first grains (fig.9a) since solidification in fact started outside the FoV. In the radiographs, these plumes are visible as darker areas because they are rich in solute and their X-ray absorption differs from the surrounding liquid at nominal composition.

The solidification front moves toward the hot part of the sample with the elongation of the first grains and from time to time the nucleation of new grains. The new solid grains float due to buoyancy force and moved back against the existing solidification front stopping the growth of existing grains (fig.9c and fig.9d) thus forming a dense and compact microstructure. The plumes were drifting continuously along the existing growth front. This visually striking feature may be attributed to the local change of the grain structure and to its permeability during the growth process, yielding to a modification of the dissipative drag force exerted on the liquid and thus on the solute plumes [88]. Similar observations were also reported by Copley *et al.* [89] or Hellawell *et al*. [90] in transparent alloys, and more recently by Boden *et al*. [91] and Shevchenko et al. [92] during upward vertical solidification of Ga-In samples or Nelson *et al.* [93] during downward solidification of Al-Cu alloys. Moreover, solidification is delayed at the root of the segregated channel due to the local increase of solute composition and the remelting of some small equiaxed grains entering the Cu-rich channel was also observed.

The impact of solute plumes on dendrite growth kinetic was analyzed by means of *in situ* X-radiography visualization, as described in details in [87]. It is possible to measure *(i)* the tip position of selected dendrites and then to determine their growth velocities as a function of time and *(ii)* the grey level in front of the dendrite tip (fig.10a). It was not possible to convert in a straightforward manner the grey level into solute concentration. However, grey-level variations in the liquid phase are representative of the change in density and composition: a brightness decrease corresponds to an enrichment of the liquid in solute, allowing a qualitative interpretation of the impact of solute concentration variations on the dendrite growth kinetic. Like in [87], it is found for the experiment presented in this paper and carried out with different solidification conditions that the dendrite tip velocity is significantly influenced by the solute plumes passing in front of the dendrites. For the dendrite indicated in fig.10a, the measurements reveal clearly the interaction between the dendrite tip growth velocity (fig.10b) and the solute

variation induced by solute plumes flows (fig.10c). The growth velocity oscillates around an average value of 10 µm/s, with a period of around 20 seconds with well-marked minima and maxima. Comparing the two plots in fig.10 highlights the close relationship between the dendrite tip growth velocity and the grey-level variation. The variations of the dendrite tip velocity are in phase with the liquid solute composition variations, and the minimum and maximum of both curves occurs roughly simultaneously (dashed lines connecting the two curves). A maximum of Cu concentration in front of the dendrite tip corresponds to a minimum of dendrite tip velocity. Moreover, in addition to the synchronization of these two curves, the oscillation amplitude is also in good accordance. The close link between dendrite tip velocity and solute plume motion ahead of the dendrite tip has been already mentioned by Shevchenko et al. [92] for the study of Ga-In, and more recently by Reinhart et al. [6] during directional solidification of superalloys. The explanation for these cycles running concurrently is that solute plumes locally increased the Cu concentration ahead of the dendrite tip, which reduces the constitutional undercooling intensity and thus slows the dendrite tip growth [94].

5. Conclusion

The aim of this paper was to give some illustrative examples showing the great interest to compare solidification experiments conducted in well-controlled conditions, on Earth and in low-gravity environment, with *in situ* and real-time characterization for both liquid aluminum alloys and transparent organic materials. It has been showed that microgravity experimentation offers a unique and efficient means for in-depth analysis of the pattern formation during directional solidification, in the limit of diffusive transport.

Obviously, *in situ* imaging methods (e.g. by optical method or X-radiography and tomography), and microgravity experimentation will play a major role in near-future work. Indeed, due to the limited microgravity opportunities afforded to date, only a very narrow range of experimental parameters have been investigated yet. It is expected that more microgravity opportunities

(sounding rockets or space stations) will be run in the future, enabling expansion in the number of cases studied, and the investigation of new phenomena. Experiments with long-duration microgravity period like the ISS would make it possible to study solidifications in steady-state conditions. It is already the case for transparent alloys with DECLIC-DSI but have to be extended to metal alloys.

Finally, it is noteworthy that, if on the one hand, *in situ* characterization provides essential information on the growth dynamics that could not be obtained by sample post-mortem analysis on the other hand, many of the studies reported above have raised new questions and opened still unexplored directions for future work in the domain of *in situ* solidification.

Acknowledgements

This work is supported by the XRMON project (AO-2004-046) of the MAP program of the European Space Agency (ESA) and by the French National Space Agency (CNES). The authors would also like to thank all the people who have contributed to these results at IM2NP (Drs G. Salloum-Jaoude, L. Abou-Khalil, H. Soltani, F. Ngomesse, J. Pereda, B. Billia). Studies with the DECLIC-DSI (Directional Solidification Insert of the DEvice for the study of Critical LIquids and Crystallization) embarked on the ISS (International Space Station) were supported by CNES (French Space Agency) and by NASA (National Aeronautics and Space Administration) Grants No. NNX12AK54G and 80NSSC19K0135.

Credit author statement:

All authors conceived and performed the experiments. All authors contributed to the experiment analysis and discussed the results. N.B., G.R. and H.N-T wrote the manuscript. F.L.M. and N.M-N provided critical feedback to the final version of manuscript. N.B. and H.N-T supervised the microgravity projects.

References

[1] H. Fredriksson and U. Åkerlind, Materials Processing during Casting, in, John Wiley & Sons, Ltd, 2006.

[2] J. A. Spittle, International Materials Reviews, 51 (2006) 247-269.

[3] M. Rappaz and P. H. Thévoz, Acta Metallurgica, 35 (1987) 1487-1497.

[4] N. J. Petch, J. Iron Steel Inst., 174 (1953) 25.

[5] E. O. Hall, Proc. Phys. Soc., London, B64 (1951) 747.

[6] G. Reinhart, D. Grange, L. Abou-Khalil, N. Mangelinck-Noël, N. T. Niane, V. Maguin, G. Guillemot, C. A. Gandin and H. Nguyen-Thi, Acta Materialia, 194 (2020) 68-79.

[7] J. W. Aveson, G. Reinhart, H. Nguyen-Thi, N. Mangelinck-Noel, A. Tandjaoui, B. Billia, K. Goodwin, T. A. Lafford, J. Baruchel, H. J. Stone and N. D'Souza, Superalloys 2012, (2012) 615-624.

[8] W. W. Mullins and R. F. Sekerka, Journal of Applied Physics, 35 (1964) 444-451.

[9] W. Kurz, D. J. Fisher and R. Trivedi, International Materials Reviews, 64 (2019) 311-354.

[10] J. D. Hunt and S. Z. Lu, Metallurgical and Materials Transactions a-Physical Metallurgy and Materials Science, 27 (1996) 611-623.

[11] N. Bergeon, D. Tourret, L. Chen, J. M. Debierre, R. Guerin, A. Ramirez, B. Billia, A. Karma and R. Trivedi, Physical Review Letters, 110 (2013) 226102.

[12] G. P. Ivantsov, Doklady Acad. Nauk. SSSR, 58 (1947) 567.

[13] J. C. Lacombe, M. B. Koss and M. E. Glicksman, Metallurgical and Materials Transactions a-Physical Metallurgy and Materials Science, 38A (2007) 116-126.

[14] S. McFadden and D. J. Browne, Computational Materials Science, 55 (2012) 245-254.

[15] W. Kurz, M. Rappaz and R. Trivedi, International Materials Reviews, (2020) 1-47.

[16] M. E. Glicksman, S. R. Coriell and G. B. McFadden, Ann. Rev. Fluid Mech., 18 (1986) 307.

[17] S. H. Davis, J. Fluid Mech., 212 (1990) 241-262.

[18] D. T. J. Hurle, Interactive Dynamics of Convection and Solidification, Kluwer Academic, Pays-Bas, 1992.

[19] H. Nguyen-Thi, G. Reinhart and B. Billia, Comptes Rendus Mécanique, 345 (2017) 66-77.

[20] H. Nguyen-Thi, Y. Dabo, B. Drevet, M. D. Dupouy, D. Camel, B. Billia, J. D. Hunt and A. Chilton, J. of Crystal Growth, 281 (2005) 654-668.

[21] A. Bogno, G. Reinhart, A. Buffet, H. Nguyen Thi, B. Billia, T. Schenk, N. Mangelinck-Noël, N. Bergeon and J. Baruchel, Journal of Crystal Growth, 318 (2011) 1134-1138.

[22] A. Bogno, H. Nguyen-Thi, A. Buffet, G. Reinhart, B. Billia, N. Mangelinck-Noël, N. Bergeon, J. Baruchel and T. Schenk, Acta Materialia, 59 (2011) 4356-4365.

[23] M. H. Burden, D. J. Hebditch and J. D. Hunt, J. Cryst. Growth, 20 (1973) 121-124.

[24] G. Salloum-Abou-Jaoude, H. Nguyen-Thi, G. Reinhart, R. H. Mathiesen, G. Zimmermann and D. Voss, Materials Science Forum, 790-791 (2014) 311-316.

[25] H. Nguyen-Thi, G. Reinhart, G. S. Abou Jaoude, R. H. Mathiesen, G. Zimmermann, Y. Houltz, D. Voss, A. Verga, D. J. Browne and A. G. Murphy, Journal of Crystal Growth, 374 (2013) 23-30.

[26] G. Salloum-Abou-Jaoude, J. Wang, L. Abou-Khalil, G. Reinhart, Z. Ren, N. Mangelinck-Noel, X. Li, Y. Fautrelle and H. Nguyen-Thi, Journal of Crystal Growth, 417 (2015) 25-30.

[27] L. Abou-Khalil, G. Salloum-Abou-Jaoude, G. Reinhart, C. Pickmann, G. Zimmermann and H. Nguyen-Thi, Acta Materialia, 110 (2016) 44-52.

[28] G. Reinhart, A. Buffet, H. Nguyen-Thi, B. Billia, H. Jung, N. Mangelinck-Noel, N. Bergeon, T. Schenk, J. Hartwig and J. Baruchel, Metallurgical and Materials Transactions a-Physical Metallurgy and Materials Science, 39A (2008) 865-874.

[29] G. Reinhart, H. Nguyen-Thi, N. Mangelinck-Noel, J. Baruchel and B. Billia, JOM, 66 (2014) 1408-1414.

[30] B. Billia, N. Bergeon, H. Nguyen Thi and H. Jamgotchian, Phys. Rev Lett., 93 (2004) 126105.

[31] S. Akamatsu and H. Nguyen-Thi, Acta Materialia, 108 (2016) 325-346.

[32] R. Trivedi, H. Miyahara, P. Mazumder, E. Simsek and S. N. Tewari, Journal of Crystal Growth, 222 (2001) 365-379.
[33] M. E. Glicksman, J. E. Frei, J. C. LaCombe, M. B. Koss, A. O. Lupulescu and C. Giummarra, Time-dependent behavior of dendrites under diffusion-controlled conditions, Springer, Dordrecht, 2001.
[34] J. C. LaCombe, M. B. Koss and M. E. Glicksman, Physical Review Letters, 83 (1999) 2997-3000.
[35] M. B. Koss, J. C. LaCombe, L. A. Tennenhouse, M. E. Glicksman and E. A. Winsa, Metallurgical and Materials Transactions a-Physical Metallurgy and Materials Science, 30 (1999) 3177-3190.
[36] B. Drevet, H. Nguyen Thi, D. Camel, B. Billia and M. D. Dupouy, J. Crystal Growth, 218 (2000) 419-433.
[37] C. C. Battalle, R. N. Grugel, A. B. Hmelo and T. G. Wang, Metallurgical and Materials Transactions A, 25 (1994) 865-870.
[38] I. Steinbach, Acta Materialia, 57 (2009) 2640-2645.
[39] A. Viardin, J. Zollinger, L. Sturz, M. Apel, J. Eiken, R. Berger and U. Hecht, Computational Materials Science, 172 (2020) 109358.
[40] G. Zimmermann, M. Hamacher and L. Sturz, Journal of Crystal Growth, 512 (2019) 47-60.
[41] K. A. Jackson and J. D. Hunt, Acta Metall., 13 (1965) 1212.
[42] R. Trivedi, Journal of Crystal Growth, 49 (1980) 219-232.
[43] M. A. Eshelman and R. Trivedi, Acta Metallurgica, 35 (1987) 2443-2452.
[44] K. Somboonsuk, J. T. Mason and R. Trivedi, Met. Trans., A15 (1984) 967.
[45] J. Deschamps, M. Georgelin and A. Pocheau, Physical Review E, 78 (2008) 011605.
[46] S. Akamatsu, G. Faivre and T. Ihle, Physical Review E, 51 (1995) 4751.
[47] M. Georgelin and A. Pocheau, Physical Review Letters, 79 (1997) 2698-2701.
[48] B. Billia, H. Jamgotchian and H. N. Thi, Journal of Crystal Growth, 167 (1996) 265-276.
[49] N. Bergeon, R. Trivedi, B. Billia, B. Echebarria, A. Karma, S. Liu, C. Weiss and N. Mangelinck, Advances in Space Research, 36 (2005) 80-85.
[50] S. Gurevich, A. Karma, M. Plapp and R. Trivedi, Physical Review E, 81 (2010) 011603
[51] F. L. Mota, N. Bergeon, D. Tourret, A. Karma, R. Trivedi and B. Billia, Acta Materialia, 85 (2015) 362-377.
[52] F. L. Mota, J. Pereda, K. Ji, Y. Song, R. Trivedi, A. Karma and N. Bergeon, Acta Materialia, 204 (2021) 116500
[53] N. Bergeon, C. Weiss, N. Mangelinck-Noel and B. Billia, Transactions of the Indian Institute of Metals, 62 (2009) 455-460.
[54] J. Pereda, F. L. Mota, J. M. Debierre, B. Billia, R. Trivedi, A. Karma and N. Bergeon, Physical Review E, 102 (2020) 032804
[55] N. Bergeon, A. Ramirez, L. Chen, B. Billia, J. H. Gu and R. Trivedi, Journal of Materials Science, 46 (2011) 6191-6202.
[56] Y. Dabo, H. Nguyen Thi, S. R. Coriell, G. B. McFadden, Q. Li and B. Billia, Journal of Crystal Growth, 216 (2000) 483-494.
[57] S. R. Coriell, G. B. McFadden, B. Billia, H. Nguyen Thi and Y. Dabo, Journal of Crystal Growth, 216 (2000) 495-500.
[58] J. Baruchel, M. Di Michiel, T. Lafford, P. Lhuissier, J. Meyssonnier, H. Nguyen-Thi, A. Philip, P. Pernot, L. Salvo and M. Scheel, Comptes Rendus Physique, 14 (2013) 208-220.
[59] H. Nguyen-Thi, L. Salvo, R. H. Mathiesen, L. Arnberg, B. Billia, M. Suery and G. Reinhart, Comptes Rendus Physique, 13 (2012) 237-245.
[60] R. H. Mathiesen, L. Arnberg, H. Nguyen-Thi and B. Billia, JOM, 64 (2012) 76-82.
[61] A. G. Murphy, R. H. Mathiesen, Y. Houltz, J. Li, C. Lockowandt, K. Henriksson, G. Zimmermann, N. Melville and D. J. Browne, Journal of Crystal Growth, 440 (2016) 38-46.
[62] C. Rakete, C. Baumbach, A. Goldschmidt, D. Samberg, C. G. Schroer, F. Breede, C. Stenzel, G. Zimmermann, C. Pickmann, Y. Houltz, C. Lockowandt, O. Svenonius, P. Wiklund and R. H. Mathiesen, Review of Scientific Instruments, 82 (2011).

[63] S. Boden, B. Willers, S. Eckert and G. Gerbeth, Visualisation of the concentration distribution and the flow field in solidifying metallic melts by means of X-ray radioscopy, in, Sheffield, U.K., 2007, pp. 311-315.
[64] A. G. Murphy, G. Reinhart, H. Nguyen-Thi, G. S. Abou Jaoude and D. J. Browne, Journal of Alloys and Compounds, 573 (2013) 170-176.
[65] C. Weiss, N. Bergeon, N. Mangelinck-Noel and B. Billia, Materials Science and Engineering a-Structural Materials Properties Microstructure and Processing, 413 (2005) 296-301.
[66] F. L. Mota, Y. Song, J. Pereda, B. Billia, D. Tourret, J. M. Debierre, R. Trivedi, A. Karma and N. Bergeon, JOM, 69 (2017) 1280-1288.
[67] A. J. Clarke, D. Tourret, Y. Song, S. D. Imhoff, P. J. Gibbs, J. W. Gibbs, K. Fezzaa and A. Karma, Acta Materialia, 129 (2017) 203-216.
[68] S. R. Coriell, D. T. J. Hurle and R. F. Sekerka, Journal of Crystal Growth, 32 (1976) 1-7.
[69] J. A. Burton, R. C. Prim and W. P. Slichter, The Journal of Chemical Physics, 21 (1953) 1987-1991.
[70] P. Lehmann, R. Moreau, D. Camel and R. Bolcato, Journal of Crystal Growth, 183 (1998) 690-704.
[71] H. Jamgotchian, N. Bergeon, D. Benielli, P. Voge, B. Billia and R. Guerin, Physical Review Letters, 87 (2001) 166105.
[72] C. Weiss, N. Bergeon, N. Mangelinck-Noel and B. Billia, Physical Review E, 79 (2009) 011605.
[73] W. A. Tiller, K. A. Jackson, J. W. Rutter and B. Chalmers, Acta Metallurgica, 1 (1953) 428-437.
[74] W. Mullins and R. Sekerka, Journal of Applied Physics, 35 (1964) 444-451.
[75] J. A. Warren and J. S. Langer, Physical Review E, 47 (1993) 2702-2712.
[76] J. J. Favier, Acta Metallurgica, 29 (1981) 205-214.
[77] D. Camel and J. J. Favier, Journal of Crystal Growth, 67 (1984) 42-56.
[78] D. Camel and J. J. Favier, Journal of Crystal Growth, 67 (1984) 57-67.
[79] D. Ruvalcaba, R. H. Mathiesen, D. G. Eskin, L. Arnberg and L. Katgerman, Acta Materialia, 55 (2007) 4287-4292.
[80] H. Jung, N. Mangelinck-Noel, H. Nguyen-Thi, N. Bergeon, B. Billia, A. Buffet, G. Reinhart, T. Schenk and J. Baruchel, International Journal of Cast Metals Research, 22 (2009) 208-211.
[81] E. Liotti, A. Lui, R. Vincent, S. Kumar, Z. Guo, T. Connolley, I. P. Dolbnya, M. Hart, L. Arnberg, R. H. Mathiesen and P. S. Grant, Acta Materialia, 70 (2014) 228-239.
[82] H. Nguyen-Thi, G. Reinhart, G. Salloum-Abou-Jaoude, D. J. Browne, A. G. Murphy, Y. Houltz, J. Li, D. Voss, A. Verga, R. H. Mathiesen and G. Zimmermann, Microgravity Science and Technology, 26 (2014) 37-50.
[83] A. Bhattacharya, Materials Research Express, 6 (2019) 126544.
[84] J. W. Gibbs, D. Tourret, P. J. Gibbs, S. D. Imhoff, M. J. Gibbs, B. A. Walker, K. Fezzaa and A. J. Clarke, Jom, 68 (2016) 170-177.
[85] B. Goyeau, D. Gobin, T. Benihaddadene, D. Gobin and M. Quintard, Metallurgical and Materials Transactions B, 30 (1999) 613-622.
[86] Y. Natsume, D. Takahashi, K. Kawashima, E. Tanigawa and K. Ohsasa, ISIJ International, 53 (2013) 838-847.
[87] H. Soltani, F. Ngomesse, G. Reinhart, M. C. Benoudia, M. Zahzouh and H. Nguyen-Thi, Journal of Alloys and Compounds, 862 (2021) 158028.
[88] A. Saad, C.-A. Gandin, M. Bellet, N. Shevchenko and S. Eckert, Metallurgical and Materials Transactions A, 46 (2015) 4886-4897.
[89] S. M. Copley, A. F. Giamei, S. M. Johnson and M. F. Hornbecker, Metallurgical Transactions, 1 (1970) 2193-2204.
[90] A. Hellawell, J. R. Sarazin and R. S. Steube, Philosophical Transactions of the Royal Society of London Series a-Mathematical Physical and Engineering Sciences, 345 (1993) 507-544.
[91] S. Boden, S. Eckert and G. Gerbeth, Materials Letters, 64 (2010) 1340-1343.
[92] N. Shevchenko, O. Roshchupkina, O. Sokolova and S. Eckert, Journal of Crystal Growth, 417 (2015) 1-8.

[93] T. Nelson, B. Cai, N. Warnken, P. D. Lee, E. Boller, O. V. Magdysyuk and N. R. Green, Scripta Materialia, 180 (2020) 29-33.
[94] L. Yuan and P. D. Lee, Acta Materialia, 60 (2012) 4917-4926.

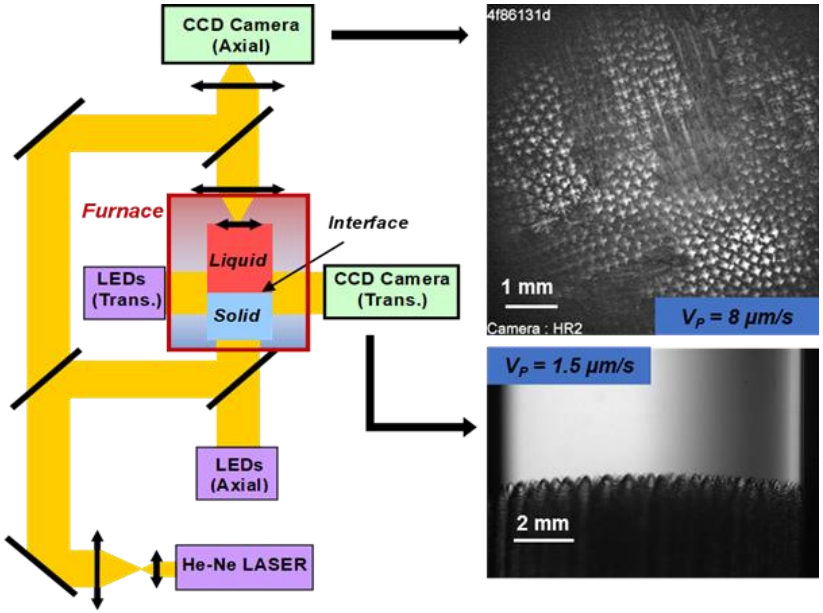

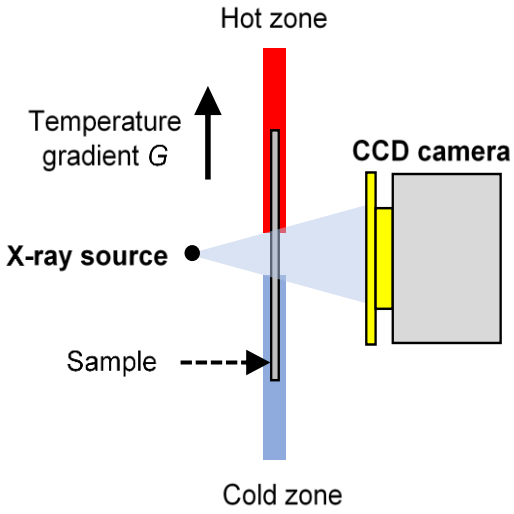

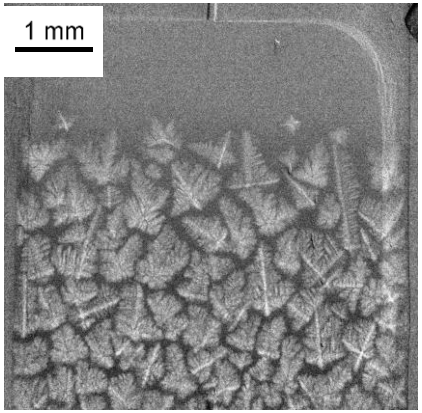

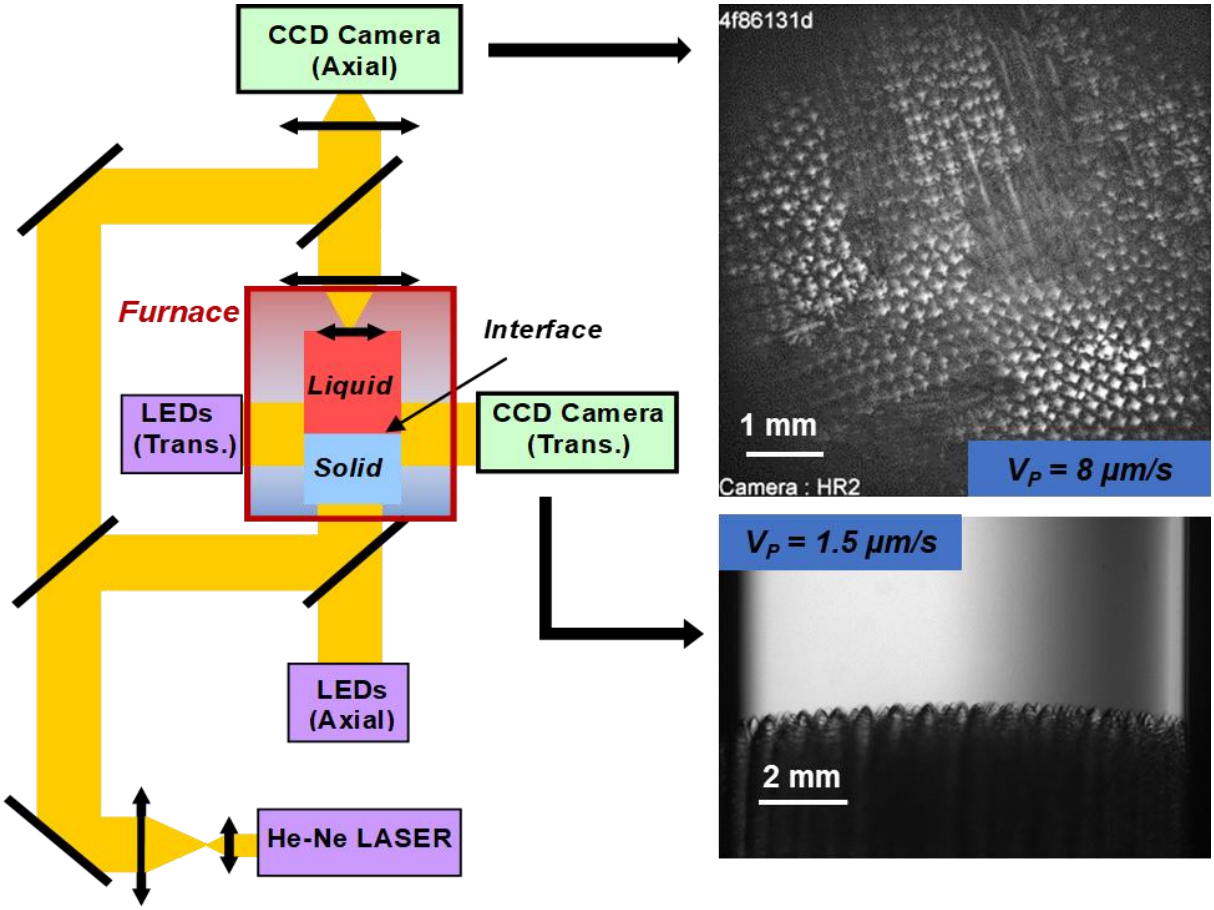

Figure 1 :

Schematic of the optical diagnostics of the DECLIC-DSI. In this scheme, the cartridge is reduced to the crucible part containing the liquid at the bottom and the solid at the top, inserted in the thermal field of the furnace. Images of axial and transverse direct observations for dendritic patterns are given as examples (Microgravity campaign onboard ISS ; SCN – 0.46 wt% Camphor ; G = 12 K/cm)

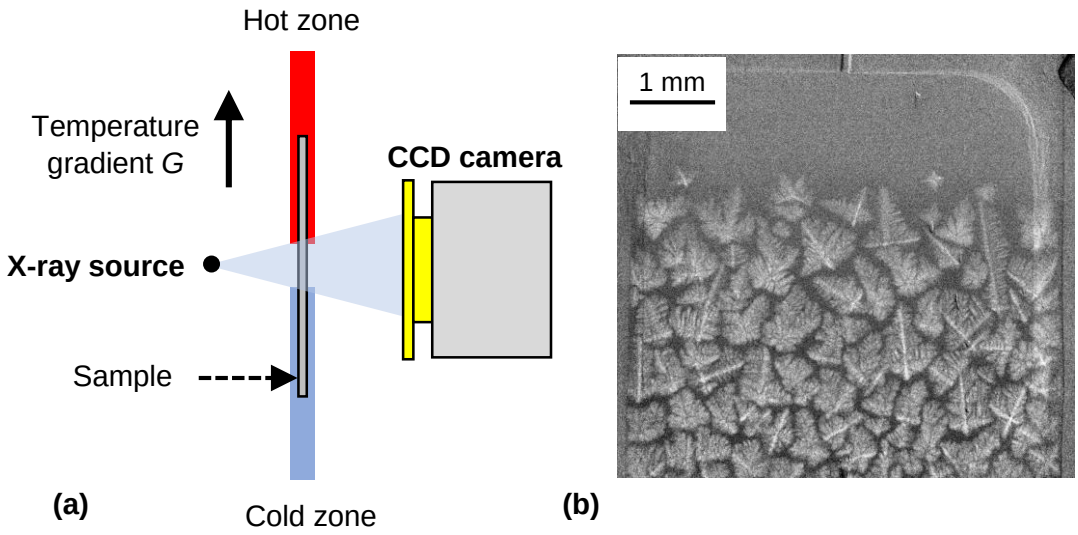

Figure 2 : (a) Schematic layout of the gradient furnace and X-radiography device developed in the framework of the ESA-XRMON project. (b) Example of radiograph recorded during the development of the microstructure in a refined Al-20wt.%Cu alloy.

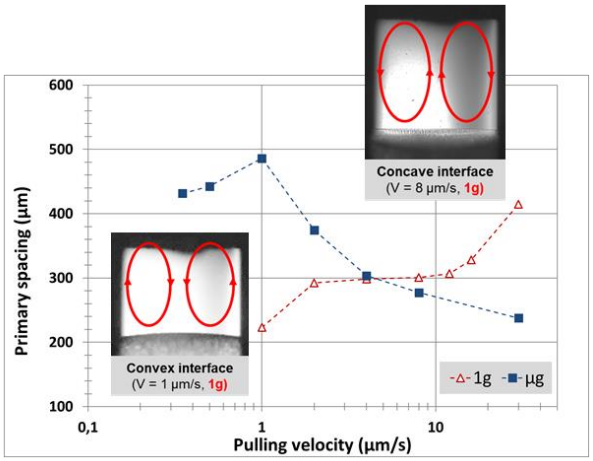

(a)

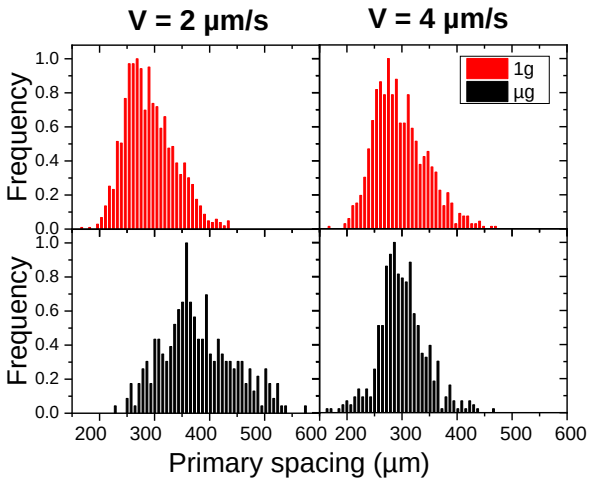

(b)

Figure 3 : (a) Primary spacing as function of pulling rate under microgravity (■) and on Earth (Δ). Insets: examples of macroscopic interface shape with corresponding convection loops. (b) Primary spacing histograms for V = 2 and 4 µm/s (G = 12 K/cm).

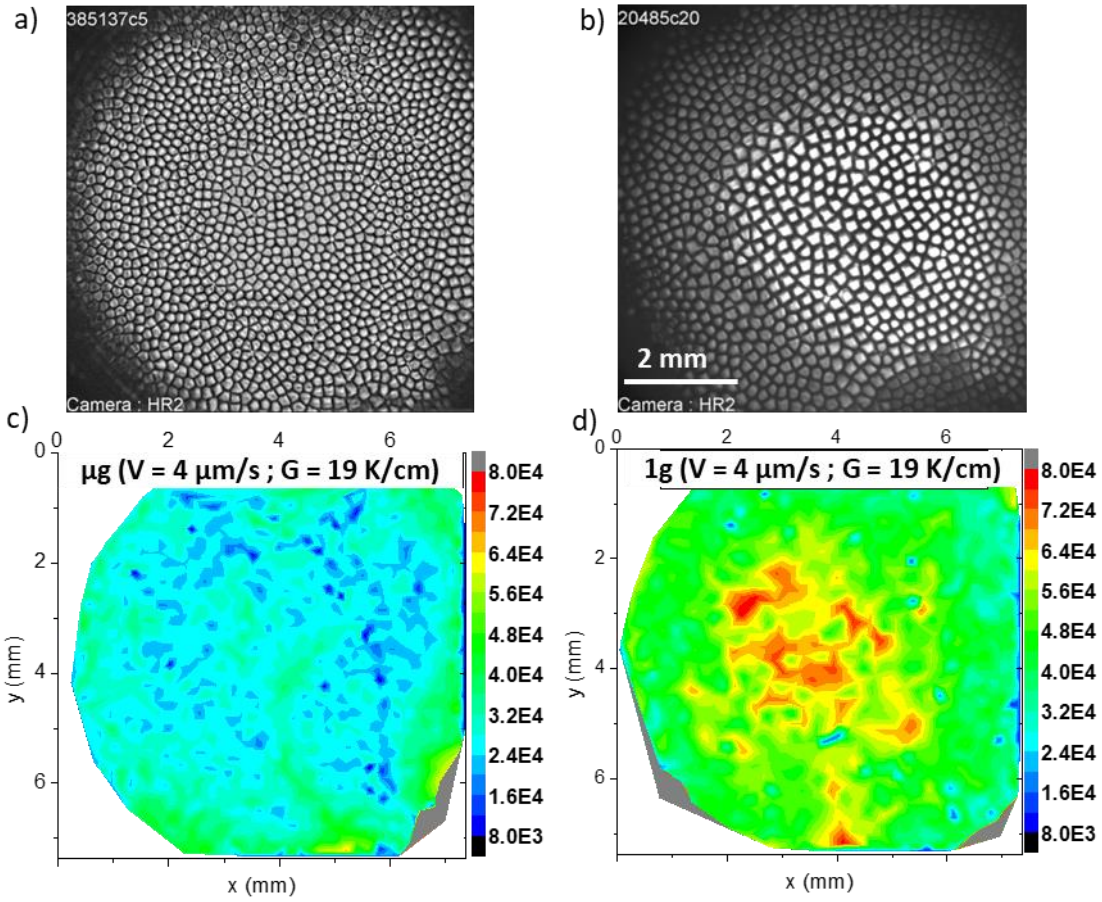

Figure 4 : a) and b) correspond to steady-state images of the cellular interface, respectively in µg and 1g, for V = 4 µm/s and G = 19 K/cm. The corresponding cell size maps (displaying the cell surface) are given respectively in c) and d). The color scale corresponds to apparent surface area given in µm².

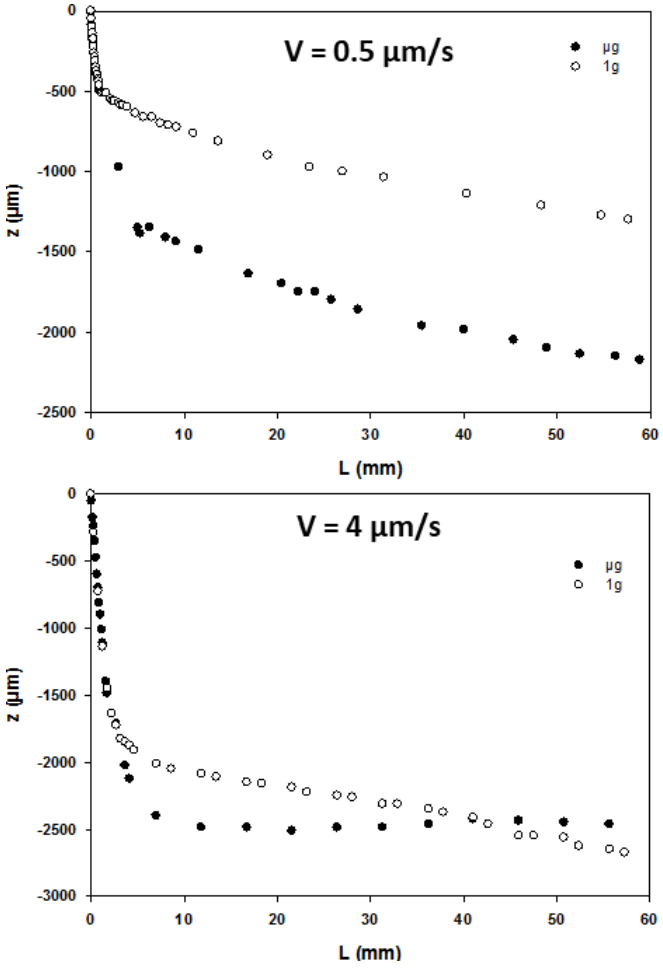

Figure 5 : Interface position as a function of solidified length ($L=Vt$) at G=12K/cm for different pulling rates onboard ISS (µg) and on ground (1g).

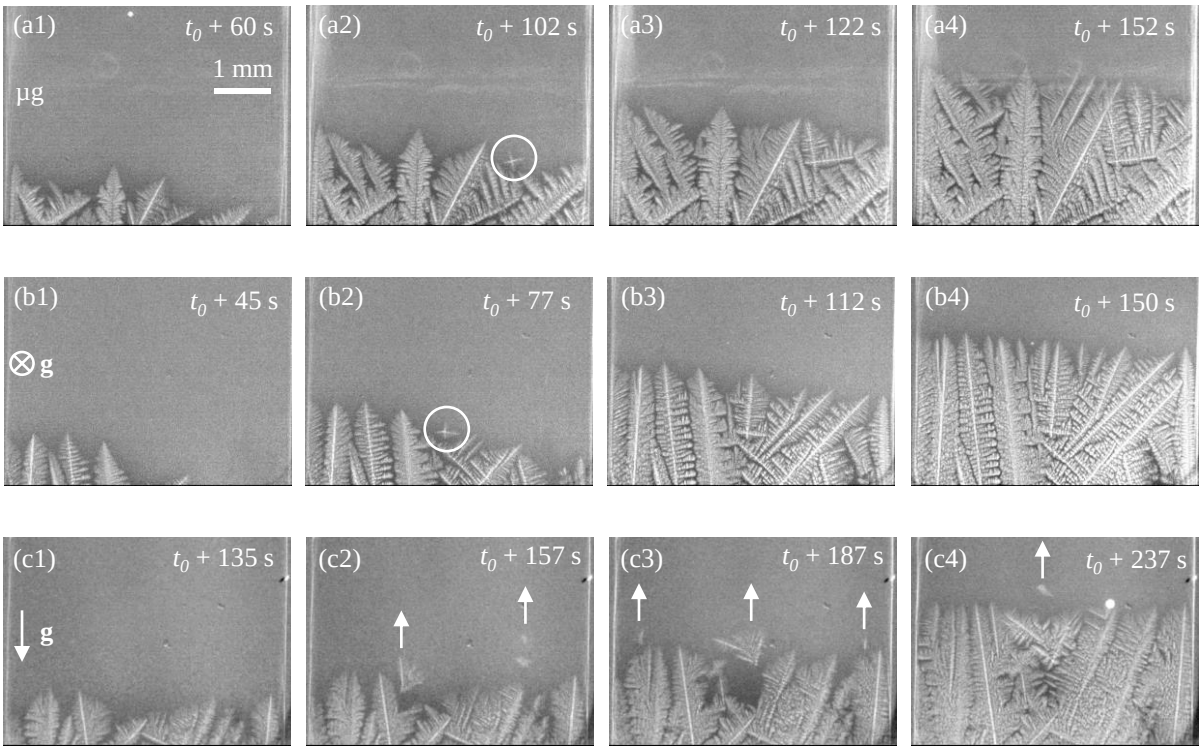

Figure 6: Columnar solidification of Al-20wt.%Cu with a temperature gradient of about 150 K/cm between the two heaters and a cooling rate of 0.15 K/s on both heaters: (a) in microgravity conditions, (b) sample in horizontal position and (c) sample in vertical position (same position of the solidification front for the three experiments). The white circles indicate grains that nucleated ahead of the solidification front. The white arrow pointing upward indicate the fragment motion. The reference time t_0 corresponds to the application of the cooling rate.

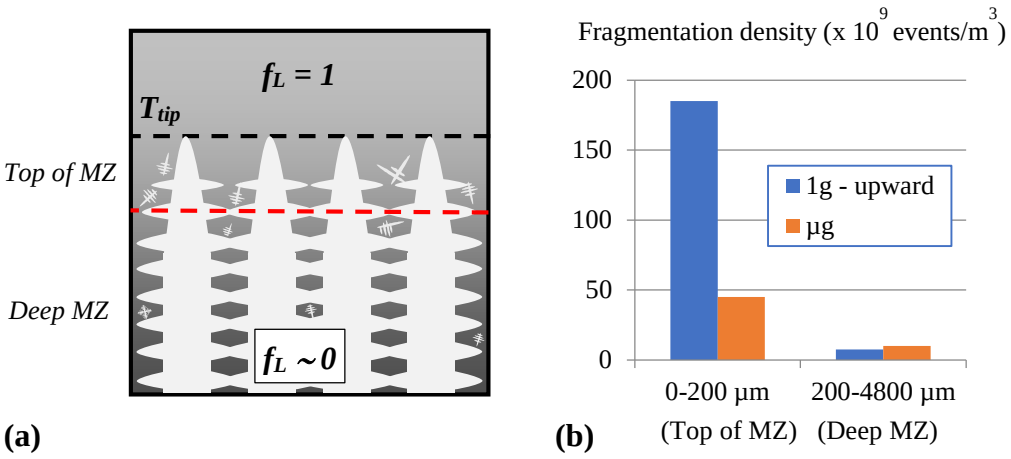

Figure 7: (a) sketch of the mushy zone (MZ) showing the so-called "top of MZ" end "deep MZ" regions, (b) Measured fragmentation density for those two regions for 1g-upward and µg experiments during columnar growth of Al-20wt%Cu alloy, in a temperature gradient G = 15 K/mm and for a cooling rate R = 0.15 K/s).

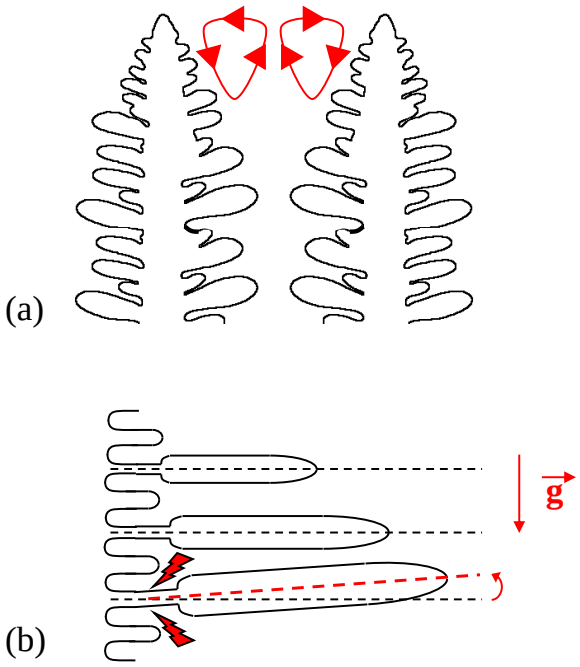

Figure 8 : Gravity effects influencing the dendrite fragmentation phenomenon: (a) natural convection in the top of the dendritic pattern and (b) buoyancy force acting on secondary arm.

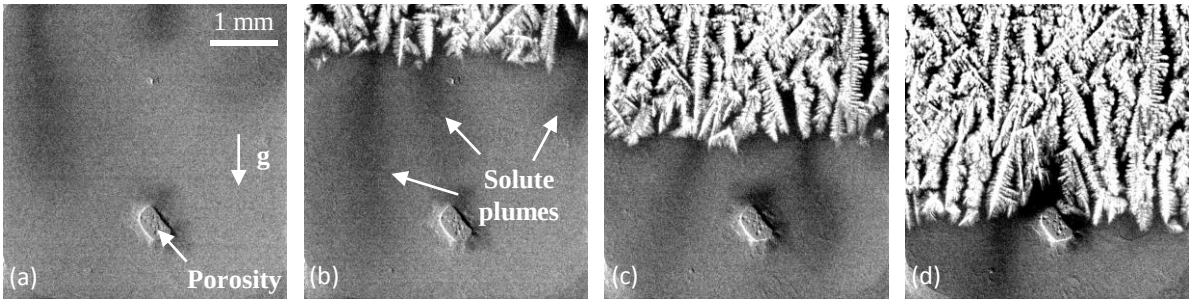

Figure 9 : Sequence of radiographs recorded during downward solidification of a refined Al-20wt.%Cu (R = 0.1 K/s and G = 7.5 K/mm) showing the propagation of the solidification microstructure from the top-cold zone toward the bottom-hot zone of the sample. The plain white arrows in (b) show solute plume locations. The reference time t = 0 s is chosen at the beginning of the temperature decrease: (a) t = 243 s, (b) t = 303 s, (c) t = 383 s, (d) t = 471 s

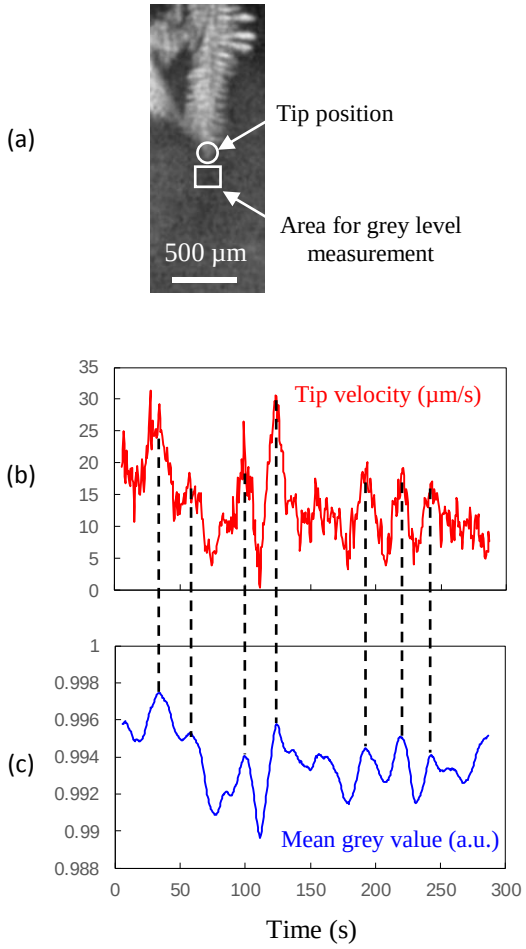

Figure 10 : (a) Sketch showing a dendrite tip position and the area used to measure the grey-level ahead of the dendrite tip. (b) Corresponding variations of the tip velocity and (c) grey level as a function of time (refined Al-20wt.%Cu, R = 0.1 K/s, G = 7.5 K/mm).